國　立　交　通　大　學

光電工程研究所

碩士論文

利用寬能隙矽氧奈米結構物製作紫外到可見光之光偵測器

Ultraviolet-visible detectors formed with wide band-gap Si-O nanostructures

研究生：枋志堯

指導教授：王興宗教受

郭浩中教授

中華民國九十五年六月

利用寬能隙矽氧奈米結構物製作紫外到可見光之光偵測器

Ultraviolet-visible detectors formed with wide band-gap Si-O nanostructures

研 究 生：枋志堯　　Student：Chih-Yao Fang

指導教授：王興宗　　Advisors：Shing-Chung Wang

郭浩中　　Hao-Chung Kuo

國 立 交 通 大 學

光 電 工 程 研 究 所

碩 士 論 文

A Thesis

Submitted to Institute of Electro-Optical Engineering

College of Electrical Engineering and Computer Science

National Chiao Tung University

in partial Fulfillment of the Requirements

for the Degree of Master

in

Electro-Optical Engineering

June 2006

Hsinchu, Taiwan, Republic of China

中 華 民 國 九 十 五 年 六 月

利用寬能隙矽氧奈米結構物製作紫外到可見光之光偵測器

研究生:枋志堯　　　　　　　　　　　　指導教授：王興宗 教授

郭浩中 教授

國立交通大學光電工程研究所碩士班

摘　要

在本論文中，我們利用寬能隙矽氧奈米結構物建構紫外到可見光之光偵測器。感應耦合式電漿化學氣相沉積系統將矽量子點合成至奈米介孔洞二氧化矽中。感應耦合式電漿使反應氣體具有高擴散率及高解離率的特性，使得矽量子點能有效率地沈積在孔壁上，因此，形成許多矽量子點/二氧化矽的結構，其密度可高達 $2.5x10^{18}/cm^3$。矽量子點/二氧化矽所形成的表面態可發出有效率的光激發螢光(PL)。藉由此介面鍵結形成寬能隙矽氧奈米結構物的特性可以增強發光效率以及光激發載子的導電性。

我們用薄膜技術在 p 型矽基板上製作寬能隙矽氧奈米結構物的方法，建構有效率的紫外光到可見光之光偵測器。此奈米結構物是由矽量子點/二氧化矽所構成。由於光激發所游離的電子會使得殘餘的電洞儲存於矽氧奈米結構物中而形成正電荷層。這樣的行為會增強逆向偏壓下光電流的產生以及些微的雪崩效應，在波長為 320-700nm 範圍內，其光響應度為 0.2-0.9A/W，增益為 1.4-2。但相對地，在順向偏壓下會造成屏蔽效應，導致順向飽和電流。

Ultraviolet-visible detectors formed with wide band-gap Si-O nanostructures

Student: Chih-Yao Fang Advisor: Dr. Shing-Chung Wang

Dr. Hao-Chung Kuo

Institute of Electro-Optical Engineering

National Chiao Tung University

Abstract

In this thesis, we constructed ultraviolet-visible detectors with wide band-gap Si-O nanostructures. The inductively coupled plasma chemical vapor deposition **(ICPCVD)** was employed to synthesize three-dimensional Si nanocrystals (NCs) within mesoporous silica films. ICP makes reactive species own highly mobile and bond with pore-wall well, therefore, efficiently construct 3D Si NCs/silica arrays. The mean density of ICP-synthesized NCs is as high as $2.5 \times 10^{18}/cm^3$. Surface states of the resulting Si NCs/silica arrays initiate blue-white photoluminescence (PL). The specific interfacial bond-induced wide-bandgap electronic structure in Si-O nanostructured film significantly enhances the light extraction efficiency and the conduction of photoexcited carriers.

We demonstrated efficient ultraviolet-visible photodiodes with blue band-gap Si-O nanostructures as capping layers on ***p*-**type silicon substrates by thin film technology. The capping layer is consisted of three-dimensional array of Si nanocrystals embedded in a mesoporous silica matrix. Hole charging in Si-O nanostructures due to photoionization of electrons forms positively charged capped layers. This occurrence enhances reverse bias of positive voltage so as to increase reverse photocurrents with responsivity of 0.2-0.9 A/W or gain of 1.4-2 in the range of 320-700 nm, in a somewhat avalanche manner, but inversely screens forward bias of negative voltage, leading to saturating forward photocurrents.

致謝

回首這兩年的研究生涯，首先感謝王興宗教授與郭浩中教授在研究方面諄諄教誨與方向的導引，王老師對學問表現出來的熱忱與執著，深深的影響了我的求學態度，也是我未來面對困難時最好的典範。再來要感謝郭浩中老師與盧廷昌老師在我論文上的建議與指導，並且時時給予我支持與鼓勵。另外，特別感謝國家奈米元件實驗室謝嘉民博士，在我研究生涯這段日子裡，指點我許多研究方向讓我學習到做事的態度及效率，使我獲益良多。

實驗製作上特別感謝奈米元件實驗室工程師賴一凡及卓恩宗學長，感謝這兩年來在實驗上的教導及提供寶貴的意見。感謝博士班學長們忻宏學長、怡超學長、小強學長、小朱學長、泓文學長、宗憲學長、小賴學長、乃方學姊在實驗上給我的協助與寶貴的建議。感謝和我一起努力兩年的同學文凱、剛帆、皇伸、柏傑、意偵、宗鼎和游敏，謝謝你們總是能在我研究期間失落的時候給我鼓勵，很高興能夠認識你們，希望未來大家還能夠常常連絡，也很謝謝學弟妹金門、孟儒、潤琪、家璞、瑞農、卓奕、碩均和秉寬的幫忙，也祝福你們未來在研究上都能順順利利的。

最後，我要感謝我親愛的父母、哥哥和妹妹，謝謝你們無怨無悔的付出與全心全力的支持，使我能順利的完成研究。

謝謝大家！也謝謝曾經幫助過我的人！

志堯　于 95 年 6 月 30 日
交通大學光電工程研究所

Contents

Abstract (in Chinese) i

Abstract (in English) ii

致謝 iii

Contents iv

List of Table vi

List of Figures vii

Chapter 1 Introduction **1**

1.1 A brief review of ultraviolet photodetectors materials 1

1.2 Review works 2

1.3 Motivation 3

1.4 References 5

Chapter 2 Theoretical Background **7**

2.1 Schottky barrier photodiodes 7

2.2 Quantum Efficiency 9

2.3 Responsivity 10

2.4 Gain 11

2.5 Response time and Bandwidth 12

2.6 Detectivity 13

2.7 References 13

Chapter 3 Experimental Detail **14**

3.1 Process 14

3.1.1 Preparation of mesoporous silica 14

3.1.2 Preparation of 3-D Si (or Ge) nanocrystals by ICP-CVD 16

3.2 Experiment Setup 18

3.2.1 Photoluminescence measurement system 18

3.2.2 Spectral responsivity measurement system 19

3.2-3 Temporal response measurement system 20

3.3 References 21

Chapter 4 Results and Discussions 22

4.1 Results of PL spectra 22

4.2 I-V characteristics of the photodetector 25

4.3 Results of Spectral response 27

4.4 Results of illumination intensity dependence of photocurrent 29

4.5 Results of temporal response 34

4.6 Discussion 35

4.7 References 38

Chapter 5 Conclusions and future works 39

5.1 Conclusions 39

5.2 Future works 40

List of Table

Table I Comparison with other researches about UV photodetectors……………….1

List of Figures

Fig.1.1 Bandgap versus the lattice constant of materials used in UV detection………1

Fig. 2.1 Four basic transport processes in forward-biased Schottky barrier on an ***n***-type semiconductor……………………………………………………...7

Fig. 3.1 Flowchart of sol-gel procedure for preparing mesoporous silica nanotemplate films……………………………………………………………………15

Fig. 3.2 Schematic mechanism of 3D Si nanodots formed by pulse ICP process…...17

Fig. 3.3 A schematic drawing illustrating the configuration of the photodiodes of ITO/nc-Si embedded MS/***p***-Si……………………………………….…17

Fig. 3.4 Diagram of photoluminescence measurement system……………..……18

Fig. 3.5 Diagram of spectral responsivity measurement system………………..……19

Fig. 3.6 Diagram of temporal response measurement system. The image shows the real measurement system………………………………………………..……20

Fig. 4.1 The cross-sectional TEM images of the mesoporous silica (MS) films with high density silicon nanocrystals and the observed distinct lattice fringes shown in the inset……………………………………………………………..23

Fig. 4.2 PL spectra of MS films embedded with nc-Si (curve a) or nc-Ge (curve b), as well as pure MS template (curve c). Inset is the naked-eye visible blue-white photoluminescence……………………………………………………………24

Fig. 4.3 Schematic of the photodiodes of ITO/nc-Si embedded MS/***p***-Si…………...26

Fig.4.4 Current-voltage characteristics of ITO/nc-Si-embedded MS/***p***-Si devices under dark and under illumination by light with intensity of 1 mW at wavelength of 325-nm, 420-nm, and 632-nm, respectively. I-V curves for the same device irradiated with 325-nm light of 3 mW and with 632-nm light of 0.3 mW were also shown…………………………………………..26

Fig. 4.5 Spectral dependence of photoresponse in ITO/nc-Si-embedded MS/***p***-Si,

ITO/MS/***p***-Si, and ITO/***p***-Si structures……………………………………28

Fig. 4.6 Current-voltage characteristics of ITO/nc-Si-embedded MS/***p***-Si devices irradiated with 325-nm light of 0.56~11.2 mW……………………………...30

Fig. 4.7 Illumination intensity dependence of photocurrent in ITO/nc-Si-embedded MS/***p***-Si devices at 325-nm light…………………………………………...30

Fig. 4.8 Current-voltage characteristics of ITO/nc-Si-embedded MS/***p***-Si devices irradiated with 632-nm light of 0.56~5.6 mW……………………………31

Fig. 4.9 Illumination intensity dependence of photocurrent in ITO/nc-Si-embedded MS/***p***-Si devices at 632-nm light…………………………………………...31

Fig. 4.10 A schematic band diagram of ITO/nc-Si-embedded MS/***p***-Si devices in equilibrium…………………………………………………………32

Fig. 4.11 Band diagram in irradiated ITO/nc-Si-embedded MS/***p***-Si under forward bias………………………………………………………………33

Fig. 4.12 Photocurrent transients of ITO/nc-Si-embedded MS/***p***-Si detectors illuminated by 420-nm, 590-nm, and 640-nm light of 1 mW…………34

Fig. 4.13 Band diagram in irradiated ITO/nc-Si-embedded MS/***p***-Si under reverse bias………………………………………………………………36

Chapter 1 Introduction

1.1 A brief review of ultraviolet photodetectors materials

Ultraviolet (UV) photodetectors are used in a wide range of applications, like flame monitoring, pollution analyzers, UV astronomy, medical instruments, or even military affairs. Recently, it attached more interests than before on being integrated with InGaN- or other-materials-based light-emitting diodes (LED) or lasers to form a base constituent for UV-blue optical storage systems. Until now, III-V semiconductors are still the main flow of the materials employed for UV detector applications, which gives a barrier for the integration with integrated circuits.

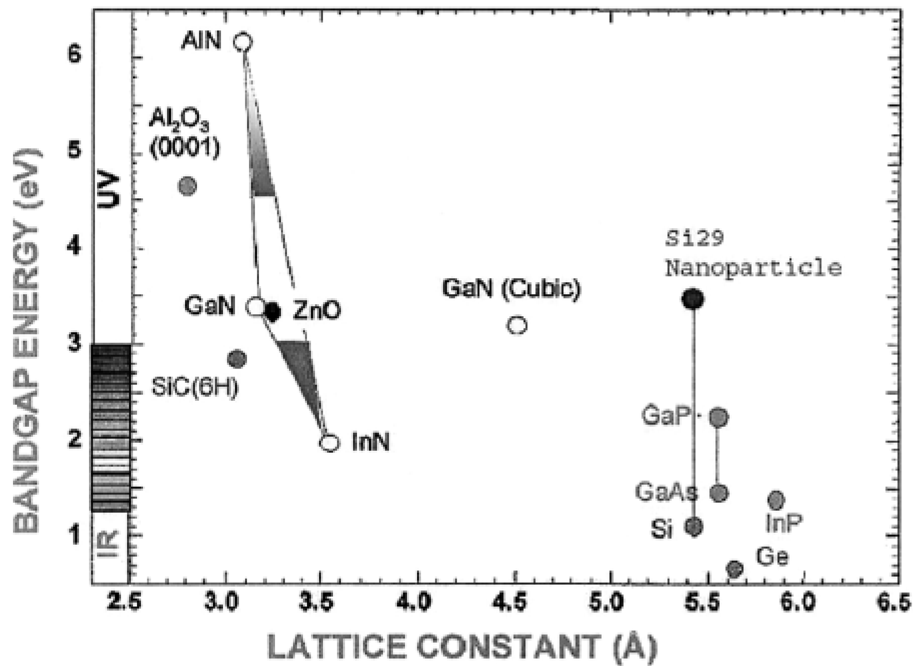

Fig.1.1 Bandgap versus the lattice constant of materials used in UV detection.

Current UV technology utilizes wide-bandgap materials, as shown in Fig. 1.1 [1]. These include metal zinc oxide and magnesium zinc oxide, III–V materials as well as Schottky-type TiO_2 UV photodiodes or GaN-AlGaN compounds [2,3]. The distinctive aspect of III–nitrides is that their bandgap are tuneable within the ultraviolet range. Other novel approaches include organics and phosphors. Silicon-based detection

utilizes silicon carbide material [4] and amorphous silicon alloys [5,6]. The many UV detectors that revolve around nitride-based heterostructures are grown on incompatible substances. Si nanoparticle-based devices may offer an opportunity for integration on Si.

1.2 Review works

Photovoltaic devices are essential components in photonics [7] and solar-cells [8], as well as even bio-chips [9]. Bulk silicon, which exhibited impressed success in electronics, with indirect narrow band-gap of 1.1 e V, fails to complete with direct wide band-gap materials on applications in ultraviolet (UV)-blue light detection, which recently face an intense demand in optical storage systems [10]. Nanostructures, unlike bulk materials, exhibited size-dependent electronic states [11]. Recent research has shown that reducing the size of a Si crystal to a few tens of atoms (1 nm) effectively creates a "direct" wide-bandgap material [12,13]. UV light couples to the particles efficiently to produce electron-hole pairs. Contrary to bulk Si or large particles, the electron hole pairs do not appreciably recombine via nonradiative processes, allowing charge separation and collection.

Specific techniques such as electrochemical etching [14,15] or porous silicon [16,17] are proposed to prepare ultrasmall Si nano-particles or nano-channels with direct wide-bandgap characteristics for Si based UV detector fabrication. With such a material, they demonstrated the Si nano-structured ultraviolet photodetector by processes which are complex, hard to be controlled, and not fully compatible with the conventional IC processing lines. Table I list the characteristics of comparison with other researches about UV photodetectors.

Material structure	Responsivity (A/W)	Detectivity (cm $Hz^{0.5}$ W^{-1})	Response time
p-AlGaN (*p-i-n*) [18]	0.13 at 354nm	3.43×10^{13}	X
GaN (MSM) [19]	0.15 at 360nm	7.24×10^{9}	X
AlGaN (MSM) [20]	0.15 at 337nm	X	0.15ns
AlGaN (MSM) [21]	0.03 at 330nm	X	5*u*s
Si-nano particles (thin film) [15]	0.85 at 365nm	$\sim 10^{12}$	~0.4*u*s

Table I Comparison with other researches about UV photodetectors.

1.3 Motivation

Since the discovery of highly efficient photoluminescence (PL) in the visible region from nanometer-sized silicon crystallites (Si nanodot) [22], extensive study on the Si nanodots has been stimulated by their possibility as a light emitting material. At the same time, the Si nanodots are expected to be a photoconductive material for the following reasons: (1) The spectral response characteristics are controlled by changing the band gap with the crystal size of the Si nanodot. (2) The impact ionization rate of the single crystal Si nanodot must be higher than that of amorphous Se and amorphous Si. (3) When a semi-ballistic carrier transport [23] in the Si-nanodot/SiO_2 system occurs, the impact ionization rate is expected to be higher than that of the single crystal Si.

In order to form Si-nanodot photoconductive films with carrier multiplication at a low electric field and photoresponse at various wavelengths, the Si nanodots with a uniform dot size distribution are necessary, because the dot size fluctuation brings about a variation in the band gap of the dots. To obtain high photosensitivity for stacked layer structures of Si nanodots, controlling the dot density and the oxide

thickness are of great importance, because the electron tunneling between neighboring Si nanodots limits the transport of the photoexcited carriers. In addition, because defects such as Si dangling bonds act as non-radiative recombination centers of the photoexcited carriers, the low defect density is also a crucial factor.

Recently, we reported that self-assembled mesoporous silica (MS) with extremely large internal surface area. The dielectric constant and reliability of MS films as interlayers strongly depend on their porosity and the amount of moisture taken up [24]. In considering the number of radiative recombination centers within the MS matrix, the porosity (or pore nanostructures) determines the total area of the pore-surfaces (and, thus, the abundances of the emission centers [25-29]) and the nanoscaled surroundings, both of which influence the luminescence efficiency and spectra. The advantages of MS film are high porosity (30~75%), controllable pore diameter (2~10nm), ordering pore channel array, and providing quantum surrounding for doping nanomaterials.

At the nanometer scale, the ratio of the numbers of atoms on the surface and in the bulk of a material increases rapidly. Interfacial properties of a nanostructures material could, therefore, enable new functional devices. In this regard, self-assembled mesoporous silica (MS) is attractive for its extremely large internal surface area and controllable nanoporous structure [30]. Recently, we showed that enhanced blue photoluminescence (PL) in three-dimensional Si nanocrystals embedded in MS had been reported [31].

In this thesis, we demonstrate a high response diode-like UV-visible detector with a capping layer of nc-Si-embedded MS. This new technology is easy and fully compatible with the IC industry on synthesizing dense, uniform, size-tunable Si NCs within mesoporous silica film as efficient far short-wavelength sensing layers. Gain in this photodiodes was found and attributed to an enhancement of reverse bias of

positive voltage by the formation of positively charged capped layer due to photoionization of electrons.

1.4 Reference

1. "European commision technology roadmap-optoelectronics interconnects for integrated circuits," Office for Official Publications of the European Communities, Luxemburg, (1998).
2. O. Katz, V. Garber, B. Meyler, G. Bahir, and J. Salzman, *Appl. Phys. Lett.* **79**, 1417, (2001).
3. S. K. Zhang , W. B. Wang F. Yun, L. He, and H. Morkoç, *Appl. Phys. Lett.* **81**, 4628, (2002).
4. D. M. Brown, E. T. Downey, M. Ghezzo, J. W. Kretchmer, R. J. Saia, Y. S. Liu, J. A. Edmond, G. Gati, J. M. Pimbley, and W. E. Schneider, *IEEE Trans. Electron Devices*, **40**, 325, (1993).
5. M. Krause, M. Topic, H. Stiebig, and H. Wagner, *Phys. Stat. Sol A*, **185**, 121, (2001).
6. J. M. Pimbley and G. J. Michon, *IEEE Trans. Electron Devices*, **34**, 294 (1987).
7. T. Takimoto, N. Fukunaga, M. Kubo, and N. Okabayashi, *IEEE Trans. Consumer Electronics*, **4**, 137 (1998).
8. Y. Mai, S. Klein, X. Geng, and F. Finger, *Appl. Phys. Lett.* **85**, 2839 (2004).
9. H. Ouyang, C. C. Striemer, and P. M. Fauchet, *Appl. Phys. Lett.* **88**, 163108 (2006).
10. F. Gan, L. Hou, G. Wang, H. Liu,and J. Li, *Materials Science and Engineering: B* **76**, 63 (2000).
11. M. V. Wolkin, J. Jorne, P. M. Fauchet, G. Allan, and C. Delerue, *Phys. Rev. Lett.* **82**, 197 (1999).
12. G. Allan, C. Delerue, and M. Lannoo, *Phys. Rev. Lett.* **76**, 2961 (1996).
13. M. H. Nayfeh, N. Rigakis, and Z. Yamani, *Phys. Rev. B* **56**, 2079 (1997).
14. O. M. Nayfeh, S. Rao, A. Smith, J. Therrien, and M. H. Nayfeh, *IEEE Photon. Technol. Lett.* **16**, 1927 (2004).
15. Munir H. Nayfeh, Satish Rao, Osama Munir Nayfeh, Adam Smith, and Joel Therrien, *IEEE Transactions on Nanotechnology*, **4**, 660 (2005).
16. J. P. Zheng, K. L. Jiao, W. P. Shen, W. A. Anderson, and H. S. Kwok, *Appl.*

Phys. Lett. **61**, 459 (1992).
17. M. K. Lee, C. H. Chu, Y. H. Wang, S. M. Sze, *Optics Letters*, **26**, 160 (2001).
18. C. K. Wang, T. K. Ko, C. S. Chang, S. J. Chang, Y. K. Su, T. C. Wen, C. H. Kuo, and Y. Z. Chiou, *IEEE Photon. Technol. Lett.* **17**, 2161 (2005).
19. C. K. Wang, S. J. Chang, Y. K. Su, Y. Z. Chiou, C. S. Chang, T. K. Lin, H. L. Liu and J. J. Tang, *Semicond. Sci. Technol.* **20,** 485 (2005).
20. N. Biyikli, I. Kimukin, B. Butun, O. Aytur, and E. Ozbay, *IEEE Journal of Selected Topics in Quantum Electronics*, **10**, 759 (2004).
21. S. K. Zhang, W. B. Wang, F. Yun, L. He, H. Morkoç, X. Zhou, M. Tamargo, and R. R. Alfano, *Appl. Phys. Lett.* **81**, 4628 (2002).
22. L. T. Canham, *Appl. Phys. Lett.* **57**, 1046 (1990).
23. N. Koshida, X. Sheng, and T. Komoda, *Appl. Surf. Sci.* **146**, 371 (1999).
24. C. M. Yang, A. T. Cho, F. M. Pan, T. G. Tsai, and K. J. Chao, *Adv. Mater.* **13**, 1099 (2001).
25. Y. D. Glinka, S. H. Lin, L. P. Hwang, and Y. T. Chen, *Appl. Phys. Lett.* **77**, 3968 (2000).
26. L. Pavesi, L. Dal Negro, C. Mazzoleni, G. Franzo, and F. Priolo, *Nature*, **408**, 440 (2000).
27. J. Y. Zhang, X. M. Bao, Y. H. Ye, and X. L. Tan, *Appl. Phys. Lett*. **73**, 1790 (1998).
28. D. P. Yu, Q. L. Hang, Y. Ding, H. Z. Zhang, Z. G. Bai, J. J. Wang, Y. H. Zou, W. Qian, G. C. Xiong, and S. Q. Feng, *Appl. Phys. Lett.* **73**, 3076 (1998).
29. M. S. EI-Shall, S. Li, T. Turkki, D. Graiver, U. C. Pernisz, and M. I. Baraton, *J. Phys. Chem.* **99**, 17806 (1995).
30. D. Y. Zhao, P. D. Yang, N. Melosh, J. G. Feng, B. F. Chmelka, and G. D. Stucky, *Adv. Mater.* **10,** 1380 (1998).
31. A. T. Cho, J. M. Shieh, J. Shieh, Y. F. Lai, B. T. Dai, F. M. Pan, H. C. Ku, Y. C. Lin, K. J. Chao, and P. H. Liu, *Electrochem. Solid-State Lett.* **8**, G143 (2005).

Chapter 2 Theoretical Background

2.1 Schottky barrier photodiodes

Schottky barrier photodiodes have been studied quite extensively and have also found application as ultraviolet detectors [1]. These devices reveal some advantages over *p-n* junction photodiodes: fabrication simplicity, absence of high-temperature diffusion processes, and high speed of response.

Current transport processes

The current transport in metal-semiconductor contacts is due mainly to majority carriers, in contrast to *p-n* junctions, where current transport is due mainly to minority carriers. The current can be transported in various ways under forward bias conditions as shown in Fig. 2.1. The four processes are: [2]

(a) Emission of electrons from the semiconductor over the top of the barrier into the metal,

(b) Quantum mechanical tunneling through the barrier,

(c) Recombination in the space-charge region,

(d) Recombination in the neutral region (equivalent hole injection from the metal to the semiconductor).

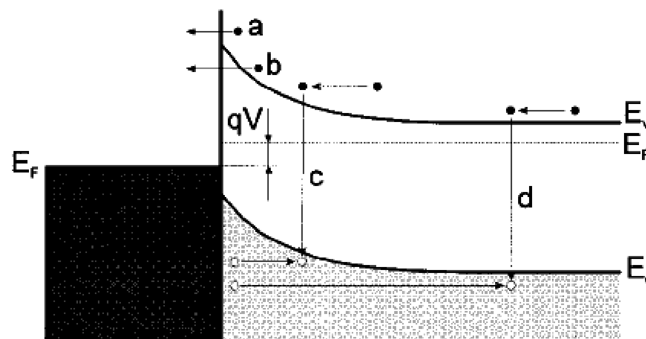

Fig. 2.1 Four basic transport processes in forward-biased Schottky barrier on an ***n***-type semiconductor.

The transports of electrons over the potential barrier have been described by various theories, namely: diffusion, thermionic emission, and unified thermionic emission diffusion. It is now widely accepted that, for high-mobility semiconductors with impurity concentrations of practical interest, the thermionic emission theory appears to explain qualitatively the experimentally observed $I-V$ characteristics. Some workers have also included in the simple thermionic theory the quantum effects (i.e., quantum mechanical reflection and tunneling of carriers through the barrier) and have tried to obtain modified analytical expressions for the current–voltage relation. This, however, has essentially led to a lowering of the barrier height and a rounding off of the top.

The thermionic emission theory by Bethe is derived from the assumptions that the barrier height is much larger than kT, thermal equilibrium is established at the plane that determines emission, and the existence of a net current flow does not affect this equilibrium. Bethe's criterion for the slope of the barrier is that the barrier must decrease by more than kT over a distance equal to the scattering length. The resulting current flow will depend only on the barrier height and not on the width, and the saturation current is not dependent on the applied bias. Then the current density of majority carriers from the semiconductor over the potential barrier into the metal is expressed as

$$J_{Mst} = J_{st}[\exp(\frac{qV}{nkT}) - 1] \tag{2.1}$$

where saturation current density

$$J_{st} = A^{*}T^{2}\exp(-\frac{q\phi_{b}}{kT}) \tag{2.2}$$

and $A^{*} = 4\pi qk^{2}m^{*}/h^{3}$ is the Richardson constant, m^* is the effective electron mass, and n is the ideality factor. Equation is similar to the transport equation for *p-n*

junctions. However, the expression for the saturation current densities is quite different.

2.2 Quantum Efficiency

The quantum Efficiency $\boldsymbol{\eta}$ $(0 \le \eta \le 1)$ is of a photodetector is defined as the probability that a single photon incident on the device generates a photocarrier pair that contributes to the detector current. When many photons are incident, as is almost always the case, $\boldsymbol{\eta}$ is the ratio of the flux of generated electron-hole pairs that contribute to the detector current to the flux of incident photons [2,4].

The quantum Efficiency is defined as

$$\eta = (1 - R)\zeta[1 - \exp(-\alpha d)] \tag{2.3}$$

where R is the optical power reflectance at the surface, ζ is the fraction of electron-hole pairs that contribute successfully to the detector current, α the absorption coefficient of the material (cm^{-1}), and ***d*** the photodetector depth.

The first factor (1-R) represents the effect of reflection at the surface of the device. Reflection can be reduced by the use of antireflection coatings. The second factor ζ is the fraction of electron-hole pairs that successfully avoid recombination at the material surface and contribute to the useful photocurrent. The third factor represents the fraction of the photon flux absorbed in the bulk of the material. The device should have a sufficiently large value of ***d*** to maximize this factor.

2.3 Responsivity

The responsivity related the electric current flowing in the device to the incident optical power. If every photon were to generate a single photoelectron, a photon flux **Φ** (photons per second) would produce an electron flux **Φ**, corresponding to a short circuit photocurrent $\boldsymbol{I_{photo}} = \boldsymbol{e}\,\Phi$. An optical power $\boldsymbol{P_{opt}} = \boldsymbol{h\,v\,\Phi}$ (watts) at frequency v would then give rise to an photocurrent $\boldsymbol{I_{photo}} = \boldsymbol{e\,P_{opt}\,/\,h\,v}$ .Since the fraction of photons producing detected photoelectrons is $\boldsymbol{\eta}$ rather than unity, the photocurrent is

$$I_{photo} = \eta e \Phi = \frac{\eta e P_{opt}}{h\nu} = RP_{opt} \tag{2.4}$$

The proportionality factor ***R***, between the photocurrent and the optical power, is defined as the responsivity ***R*** of the device. ***R*** has units of A/W and is given by

$$R = \frac{I_{photo}}{P_{opt}} = \frac{\eta e}{h\nu} = \eta \frac{\lambda_o}{1.24} \quad (\frac{A}{W}) \quad \lambda_o \ in \ \mu m \tag{2.5}$$

R increases with $\boldsymbol{\lambda_o}$ because photoelectric detectors are responsive to the photon flux rather than to the optical power. As $\boldsymbol{\lambda_o}$ increases, a given optical power is carried by more photons, which, in turn, produce more electrons. The region over which R increases with $\boldsymbol{\lambda_o}$ is limited, however, since the wavelength dependence of $\boldsymbol{\eta}$ comes into play for both long and short wavelengths.

2.4 Gain

The formulas presented above are predicated on the assumption that each carrier produces a charge ***e*** in the detector circuit. However, many devices produce a charge ***q*** in the circuit that differs from ***e*** [4]. Such devices are said to exhibit gain. The gain ***G*** is the average number of circuit electros generated per photocurrent pair. ***G*** should be distinguished from η, which is the probability that an incident photon produces a detectable photocurrent pair. The gain, which is defined as

$$G = \frac{q}{e} \tag{2.6}$$

can be either greater than or less than unity. Therefore, more general expressions for the photocurrent and responsivity are

$$I_{photo} = \eta \Phi q = G \eta \Phi e = \frac{G \eta e P}{h \nu} \tag{2.7}$$

and

$$R = \frac{G \eta e}{h \nu} = G \eta \frac{\lambda_o}{1.24} \qquad \lambda_o \ in \ \mu m \tag{2.8}$$

respectively.

The responsivity of a photoconductor is given by (2.8). The device exhibits an internal gain which, simply viewed, comes about because the recombination lifetime and transit time generally differ. Suppose that electrons travel faster than holes and that the recombination lifetime is very long. As the electron and hole are transported to opposite sides of the photoconductor, the electron completes its trip sooner than the hole. The requirement of current continuity forces the external circuit to provide another electron immediately, which enters the device from the wire at the left. This new electron moves quickly toward the right, again completing its trip before the hole reaches the left edge. This process continues until the electron recombines with the hole. A single photon absorption can therefore result in an electron passing

through the external circuit many times. The expected number of trips that the electron makes before the process terminates is [3]

$$G = \frac{\tau}{\tau_e} \tag{2.9}$$

Where $\boldsymbol{\tau}$ is the excess-carrier recombination lifetime and $\boldsymbol{\tau_e}$ is the electron transit time across the sample. The charge delivers to the circuit by a single electron-hole pair in this case is $\boldsymbol{q = G\,e > e}$ so that the device exhibits gain.

2.5 Response time and Bandwidth

The frequency response of a photodiode may be determined by basically three effects: [2]

(1) the time of carrier diffusion to the junction depletion region, $\boldsymbol{\tau_d}$;

(2) the transit time of carrier drift across the depletion region, $\boldsymbol{\tau_e}$;

(3) the ***RC*** time constant, $\boldsymbol{\tau_{RC}}$ associated with circuit parameters including the junction capacitance ***C*** and the parallel combination of diode resistance and external load (the series resistance is neglected).

The response time of photoconductor detectors is, of course, constrained by the transit time and ***RC*** time-constant. The carrier-transport response time is approximately equal to the recombination time $\boldsymbol{\tau}$, so the carrier-transport bandwidth ***B*** is inversely proportional to $\boldsymbol{\tau}$. Since the gain ***G*** is proportional to $\boldsymbol{\tau}$ in accordance with (2.9), increasing $\boldsymbol{\tau}$ increases the gain, which is desirable, but it also decreases the bandwidth, which is undesirable. Thus the gain-bandwidth product ***GB*** is roughly independent of $\boldsymbol{\tau}$.

As a final point, we mention that photodetectors of a givens material and structure often exhibit a fixed gain-bandwidth product. Increasing the gain results in a decrease of the bandwidth, and vice versa. This trade-off between sensitivity and

frequency response is associated with the time required for the gain process to take place.

2.6 Detectivity

The specific detectivity ***D**** for a photodetector, a figure of merit used to characterize performance, is equal to

$$\frac{e\eta}{h\nu}\sqrt{\frac{R_o A}{4kT}} \tag{2.10}$$

where e is the electronic charge, η is the quantum efficiency, h is Planck's constant, ν is the frequency of the radiation, Ro is the dynamic resistance at zero bias, A is the detector area, k is Boltzman's constant, and T is the absolute temperature [5].

2.7 References

1. David Wood, "*Optoelectronic Semiconductor Devices*", (Prentice Hall, New York, 1994).
2. M. Razeghi and A. Rogalski, *J. Appl. Phys.* 79, 7433 (1996).
3. S. M. Sze, *Physics of Semiconductor Devices*, 2nd ed. (Wiley, New York, 1981), pp.743-770.
4. Bahaa E. A. Saleh and Malvin Carl Teich, "*Fundamentals of Photonics*", (Wiley-Interscience Publication, New Yok, 1991).
5. C. K. Wang, T. K. Ko, C. S. Chang, S. J. Chang, Y. K. Su, T. C. Wen, C. H. Kuo, and Y. Z. Chiou, *IEEE Photon. Technol. Lett.* **17**, 2161 (2005).

Chapter 3 Experimental Details

3.1 Process

3.1.1 Preparation of mesoporous silica

The mesoporous silica (MS) nanotemplate films [1] were fabricated on p-type silicon substrates by using spinning-coating. The precursor solution was prepared by adding an ethanol solution of triblock copolymer Pluronic P123 (**P123**) to the silica sol-gel, which was made by refluxing a mixture of tetraethylorthosilicate (TEOS), H_2O, HCl, and ethanol at 60~80℃ for 60~120 min. The molar ratios of reactants were 1:0.008-0.03:3.5-5:0.003-0.03:10-34 (TEOS/P123/H_2O/HCl/ethanol). After the precursor solution was aged at room temperature for 3~6 hors under ambient conditions, it was spin-coated onto silicon substrates at 3000 rpm for 30 seconds. Finally, the coated film was dried ar 40~60℃ for 4~6 hours, and then baked ar 100~120℃ for 3 hours. The resultant mesoporous silica film was employed as nanotemplate for the growth of three-dimensional array of Si (Ge) nanocrystals (nc). The flowchart of sol-gel procedure for preparing mesoporous silica nanotemplate films is shown in Fig. 3.1.

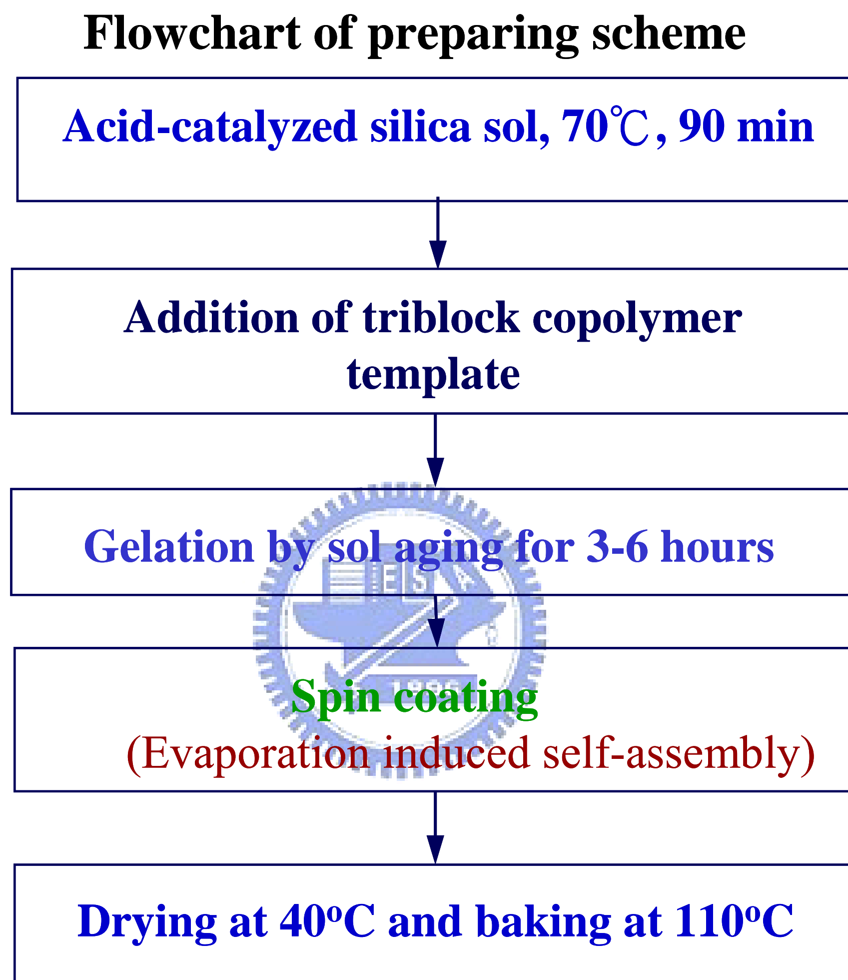

Fig. 3.1 Flowchart of sol-gel procedure for preparing mesoporous silica nanotemplate films.

3.1.2 Preparation of 3-D Si (or Ge) nanocrystals by ICP-CVD

Nc-Si (or nc-Ge) was growth by inductively coupled plasma chemical vapor deposition **(ICPCVD)** [2,3] on a cluster-level system with base pressure as low as 10^{-6} Torr. After loading MS-coated wafers into the chamber, the mixture plasma at 500W was powered on, while keeping the pressure below 10mtorr and substrate temperature at 400℃ during the entire process. MS films embedded with high density silicon (or germanium) nanocrystals were prepared by using ten cycles of pulsed SiH_4+H_2/H_2(or GeH_4+H_2/H_2) ICP with a duty cycle of 1 second/ 5 seconds.

Mechanism of 3-D NCs-synthesis

The formation of nc-Si (or nc-Ge) in the nanopores of the MS matrices using a pulse plasma involves numerous reactions. Firstly, the pure-H_2-ICP-plasma (step A of Fig. 3.2) removes organic-templates of MS matrices lightly for enabling limited nucleation sites of Si-OH on pure-surfaces [4]. This is a self-limiting reaction (SLR), which is a core concept in atomic layer deposition [5]. Sequentially, ICP-dissolved SiH_x (GeH_x) species (step B of Fig. 3.2) in the form of nanoclusters diffuse into the nanopores, and are then absorbed and embedded in the residual organic-template of MS. They eventually react with the nucleation sites through hydrogen-elimination reaction (HER). Therefore, both self-limiting reaction [5] and hydrogen-elimination reaction (HER) [4,5] govern the conversion of ICP-dissolved species in MS into nc-Si (or nc-Ge). The density of nc-Si (or nc-Ge) grown by pulsed plasma can as high as $2.5 \times 10^{18}/cm^3$.

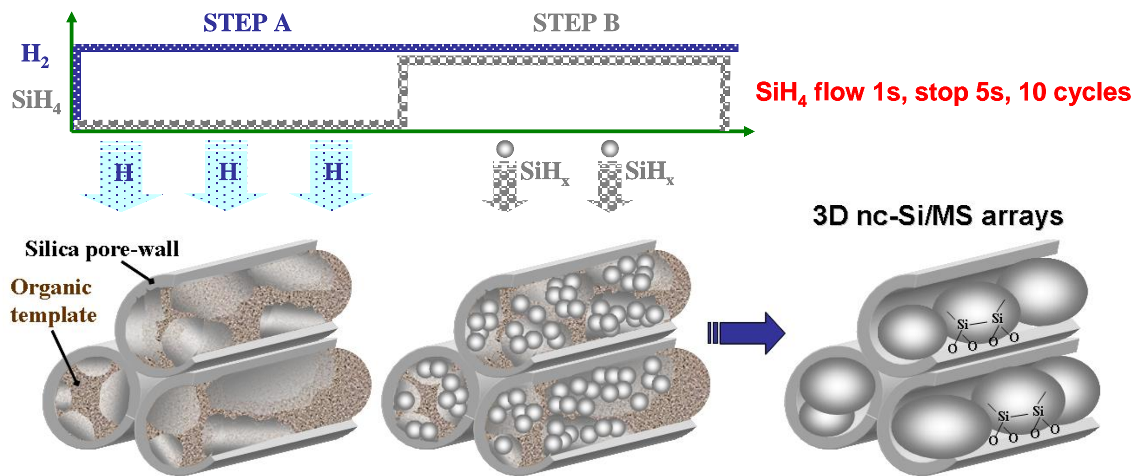

Fig. 3.2 Schematic mechanism of 3D Si nanodots formed by pulse ICP process.

For device applications, the organic contents of MS are removed by calcinations in the same chamber with H_2 plasma at the flow rate of 200 sccm for 10 minutes. The indium–tin–oxide (ITO) films of 2400A° thick were deposited onto the samples (2x2.5mm^2) by E-gun evaporation, followed by 20 min of annealing at 400℃ in N_2 ambient. A schematic structure of the photodetector is shown in Fig. 3.3.

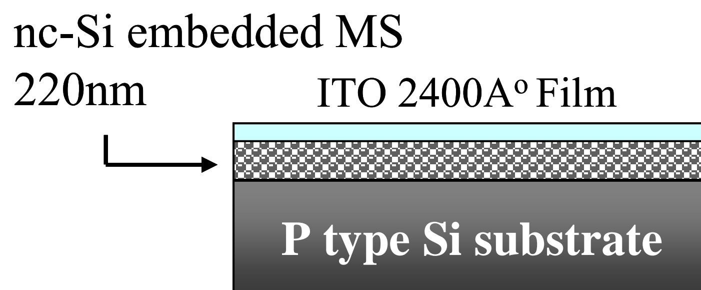

Fig. 3.3 A schematic drawing illustrating the configuration of the photodiodes of ITO/nc-Si embedded MS/***p***-Si.

3.2 Experiment Setup

3.2.1 Photoluminescence measurement system

The setup of our PL system is shown in Figure 3.4. The excited light source is continuous wave Helium-Cadmium Laser which is manufactured by Melles Griot Company. Its main peak is 325 nm. This multimode laser is no particular polarization and its output power is 30 mW. Laser focuses on the sample through three reflectors and a focal lens which focal length is five centimeter. The spot diameter is about 0.3 mm after focusing and the power density reaches 21 W/cm^2 on the surface of the sample. The excited luminescence of the sample is also through this focal lens which forms the confocal route with another focal lens in front of the spectrometer.

The type of the spectrometer is Jobin-Yvon Triax-320 monochromator. It includes three kinds of gratings and the stripe density per centimeter are 1200, 1800, and 300 respectively. In the measurement, we use that the stripe density is 1200 grooves/mm grating and the slit of 0.2 mm. Under these conditions, the resolution is about 4 Å. In order to avoid laser entering the spectrometer directly, we place a wavelength filter which filters wavelengths under 360 nm in front of the spectrometer. At the exit of the spectrometer Triax 320, a high sensitive Hamamatsu photomultiplier tube (PMT) with GaAs photocathode was placed to detect the signals.

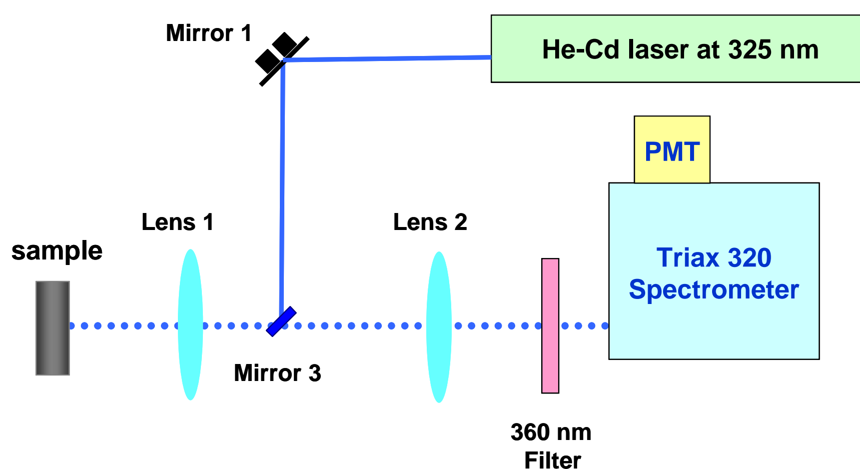

Fig. 3.4 Diagram of photoluminescence measurement system

3.2.2 Spectral responsivity measurement system

The setup of spectral responsivity measurement system as showed in Fig. 3.5. Spectral responsivity measurements were achieved using a 300 W xenon lamp with wavelength selection using a double-grating monochoramator (Jobin-Yvon Gemini 180). Lamp focuses on the sample through a focal lens which focal length is five centimeter and a fluorescence microscope. The spot diameter is about 2 mm after focusing and the power is 0.3~2 mW on the surface of the sample. The measurements of current-voltage characteristics were controlled by the Labview programs. A Keithley 2400 source measurement unit was used to apply biases to the electrodes. In dc mode, bias-dependent responsivity was measured by recording current–voltage (I –V) curves under a fixed wavelength. The power density of the excitation was determined with a calibrated UV Si photodetector.

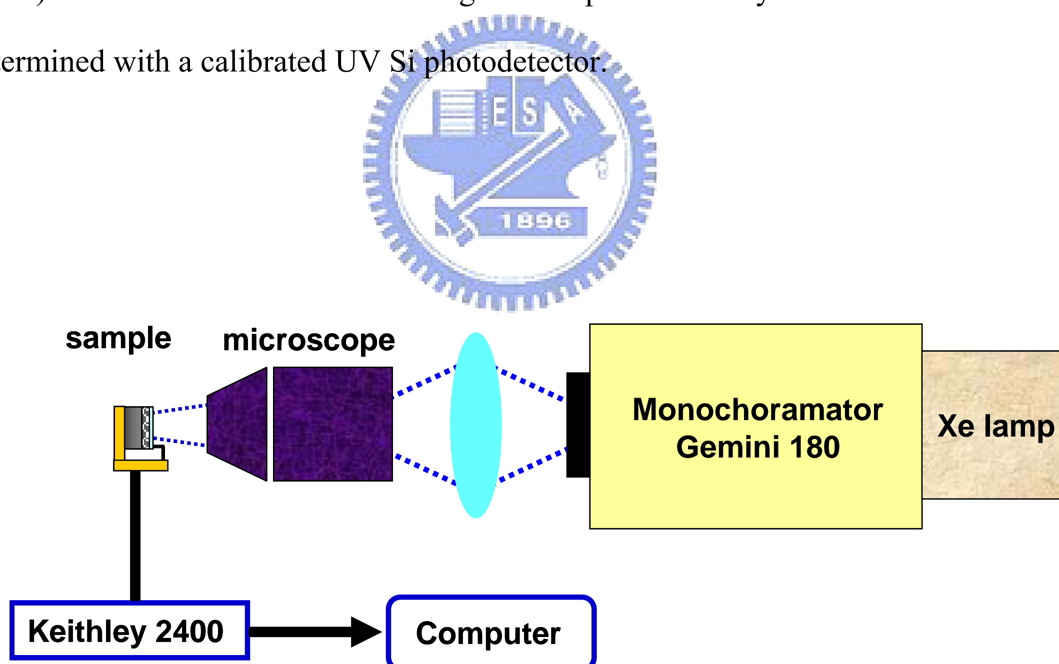

Fig. 3.5 Diagram of spectral responsivity measurement system

3.2-3 Temporal response measurement system

The setup of temporal response measurement system as showed in Fig. 3.6. The temporal response of the detectors was characterized using a third harmonic at 355nm of a mode-locked picosecond Nd: YAG laser (Ekspla, PL-2143, 24ps, 10Hz) with optical parametric generation and different frequency generation units (Ekspla, PG401-DFG) to generate tunable visible to IR pulses with pulse width of 5ps. The incident laser power was sufficiently attenuated to avoid any artificial decrease of decay times due to saturation effects. The photocurrent decay across a load resistance of 50Ωin series with the detector was measured at the applied bias. The transient output signal was then coupled to a bias tee (200 kHz~6 GHz) and displayed by a digital oscilloscope with a 500 MHz bandwidth.

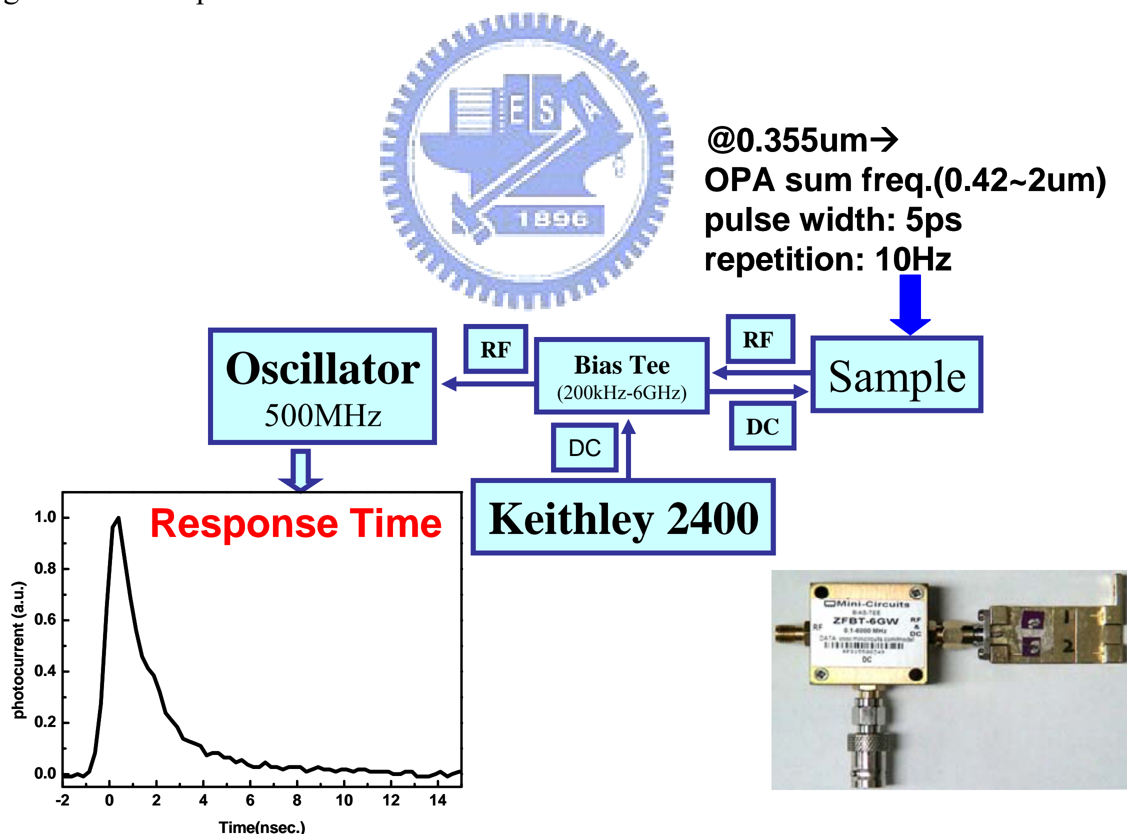

Fig. 3.6 Diagram of temporal response measurement system. The image shows the real measurement system.

3.3 References

1. D. Zhao, P. Yang, N. Melosh, J. Feng, B. F. Chmelka, and G. D. Stucky, *Adv. Mater.* **10**, 1380 (1998).
2. J. M. Shieh, K. C. Tsai, and B. T. Dai, *Appl. Phys. Lett.* **81**, 1294 (2002).
3. J. H. Wu, J. M. Shieh, B. T. Dai, and Y. S. Wu, *Electrochemical and Solid-State Letters* **7 (6)**, G128 (2004).
4. Ö. Dag, G. A. Ozin, H. Yang, C. Reber, and G. Bussi`ere, *Adv. Mater.* **11**, 474 (1999).
5. Y. J. Lee, and S. W. Kang, *Electrochemical and Solid-State Letters*, **6 (5),** C70 (2003).

Chapter 4 Results and Discussions

4.1 Results of PL spectra

Interfacial bonding-induced wide-bandgap materials

The experiment was started with the formation of a 220-nm-thick MS template layer on *p*-type silicon substrates. Si or Ge nanocrystals were thereafter synthesized in the MS templates by using a plasma technique [1]. Fig. 4.1 is the cross-sectional transmission electron microscopy (TEM) image for the sample. One can see that the MS film decorated with 2.5×10^{18} cm^{-3} of Si nanocrystals, and the mean sizes of nc-Si was found to be 4 nm.

The PL spectrum of such a nanostructured film shown in Figure 4.2 exhibit a broad-band emission at 2.7 eV (λ=460 nm). Three peaks (415, 460 and 580 nm) on the PL spectrum of nc-Si embedded MS films are attributable to the radiative defects of two-fold-coordinated silicon lone-pair center-related species (SLP) [Si:] [2,3], neutral oxygen vacancies (NOV) [≡Si-Si≡] [2-4], and nonbridging oxygen hole centers (NBOHC) [≡Si-O•] [5], respectively. Note that the three peaks were also observed on pure MS template [1,6] and nc-Ge-embedded MS [1], but with incorporation of nc-Si (Ge) this BB emission was much more enhanced. The PL intensity of nc-Si embedded MS is about one hundred times than the pure MS template. We therefore conclude that this BB emission would not be due to nanocrystals, but was rather related to the MS layer. Similar spectra of the 460 nm PL emission band were previously reported by Zhang *et al.*, and was assigned due to the interfacial states associated with neutral defects of oxygen vacancy (≡Si-Si≡) [4]. This interpretation could then be applied to our case as well, meaning that such a type of oxide defects might exist in these MS films, while for obtaining the high PL intensity it requires an efficient pumping mechanism. The semiconductor nanocrystals,

however, also play a role by sensitizing the blue emission through generating more photoexcited carriers. These carriers are then trapped in the interfacial oxygen defects and recombine to increase the intensity of the peak 460-nm PL.

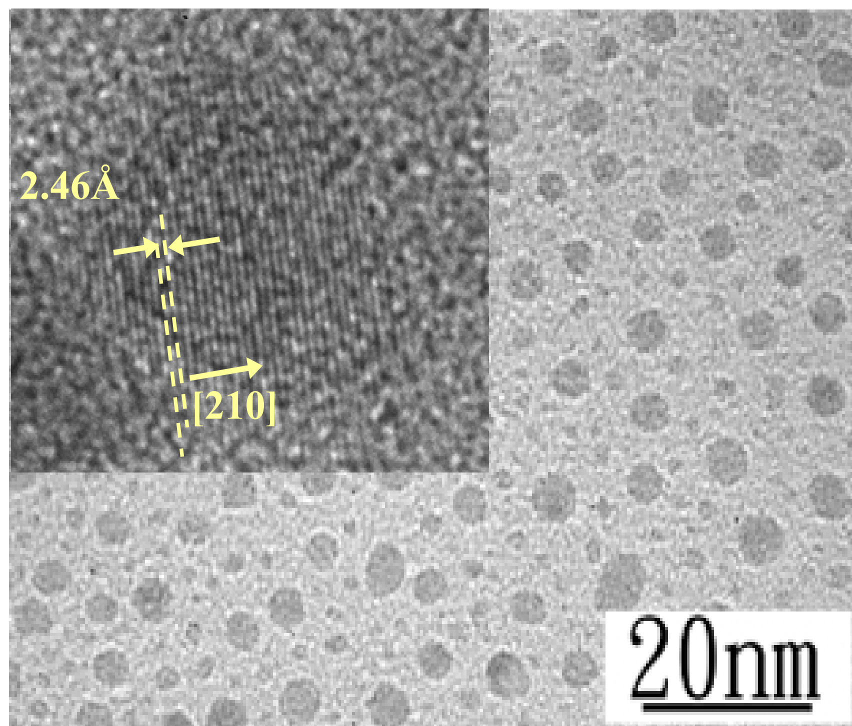

Fig. 4.1 The cross-sectional TEM images of the mesoporous silica (MS) films with high density silicon nanocrystals and the observed distinct lattice fringes shown in the inset.

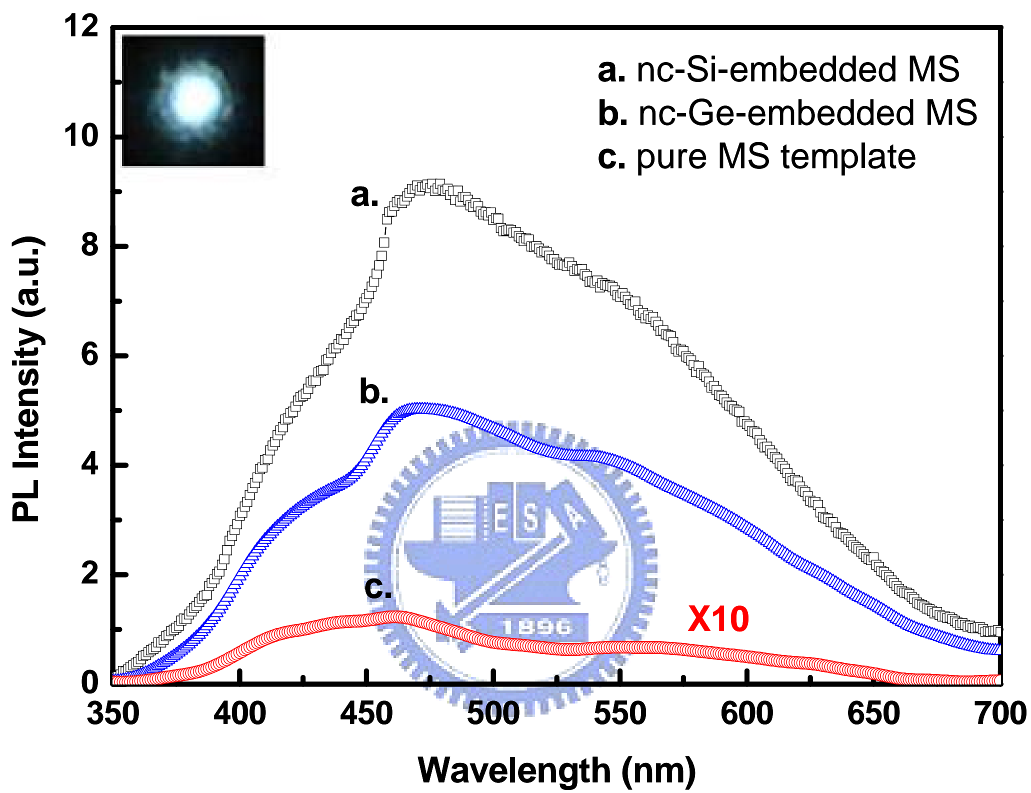

Fig. 4.2 PL spectra of MS films embedded with nc-Si (curve a) or nc-Ge (curve b), as well as pure MS template (curve c). Inset is the naked-eye visible blue-white photoluminescence.

4.2 I-V characteristics of the photodetector

For light detection, a top electrode of indium–tin–oxide (**ITO**) electrodes of 2x2.5 mm^2 is thus formed on samples to conduct (collect) an external bias (photocurrent) and to allow light transmission. A schematic structure of the photodetector is shown in Figure 4.3.

Figure 4.4 shows current-voltage (***I-V***) characteristics of this ITO/nc-Si embedded MS/***p-***Si device under dark conditions, which reveals a rectifying behavior with rectifying ratio of 87 and dark current density as low as 1.6×10^{-6}A /cm^2 at 3 V. In the range of low forward bias of 0 V to -0.9 V, the ***I-V*** characteristic is fairly described by a serial combination of a diode (ideality factor~2.1) and resistor (75 KΩ) [7]. Over this range, a space-charged-limited current (~$V^{1.77}$) dominates ***I-V*** characteristics [8]. Studies on carrier transport in the metal/Si nanostructures (porous Si or Si nanoparticle films)/Si configuration indicated that high density of states in nanostructures results in ohmic manner at metal/nanostructure interface and a diodelike behavior at the nanostructure/Si interface. Therefore, the reverse current is limited by the diode barrier [9]. Under forward bias, current flow through the resistor of nanostructures is strongly field-dependent [10], which relation is consistent with the ***I-V*** characteristic of ITO/nc-Si-embedded MS/***p-***Si structure.

Figure 4.4 also plots ***I-V*** curves of our device irradiated by light with wavelength of 425-nm and 632-nm, and with illumination intensity of 1 mW. Under forward bias (0 V to -6 V), all currents starts to rise at -0.5 V, and reaches 0.26 mA and 0.3 mA at -5 V, respectively. In comparison, under reverse bias (0 V to 6 V), currents starts to rise at larger voltage of 1.5 V, then linearly increase with bias voltage, before saturating at 0.4 mA and 0.6 mA when bias voltage was above 4 V, respectively. As illumination intensity increases, reverse currents continuously enlarge, whereas forward currents exhibit a saturating behavior, as seen on Fig. 4.4. Therefore, in

illuminated samples, a reversal in rectifying behavior occurs.

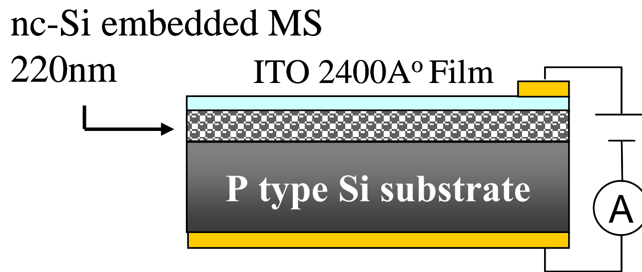

Fig. 4.3 Schematic of the photodiodes of ITO/nc-Si embedded MS/***p***-Si.

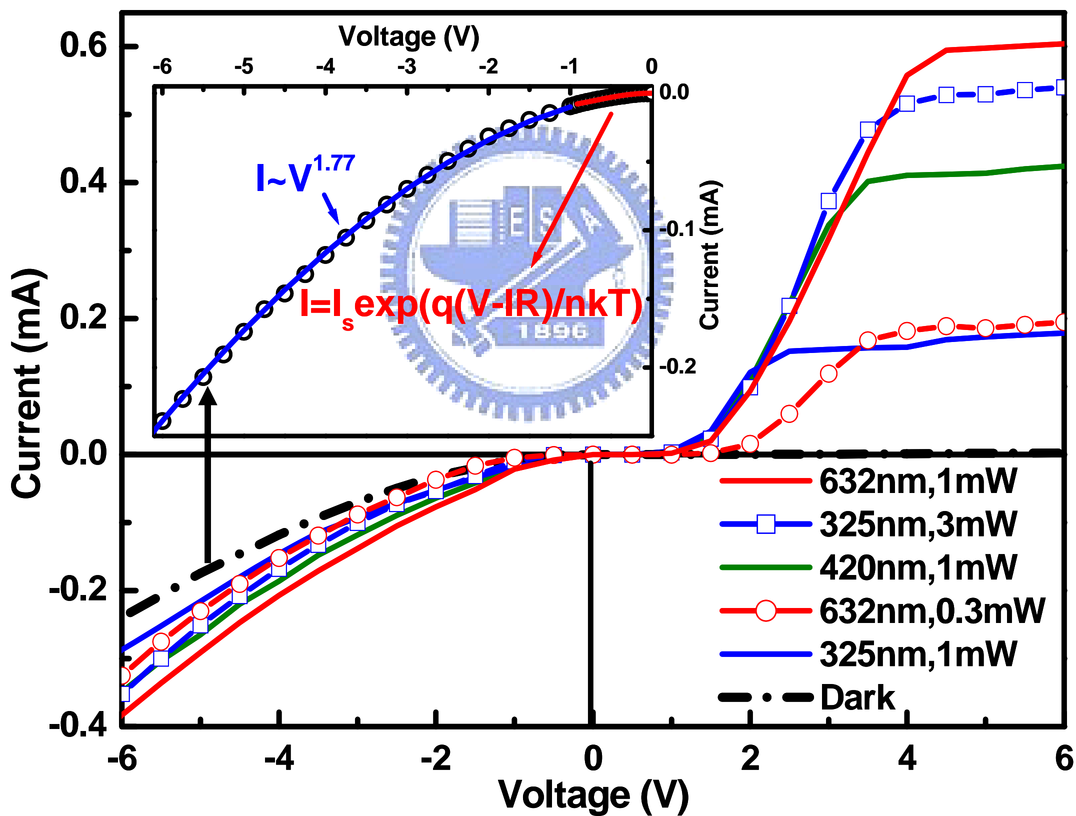

Fig.4.4 Current-voltage characteristics of ITO/nc-Si-embedded MS/***p***-Si devices under dark and under illumination by light with intensity of 1 mW at wavelength of 325-nm, 420-nm, and 632-nm, respectively. I-V curves for the same device irradiated with 325-nm light of 3 mW and with 632-nm light of 0.3 mW were also shown.

4.3 Results of Spectral response

Figure 4.5 further shows spectral dependence of photoresponse in ITO/nc-Si-embedded MS/***p***-Si, ITO/MS/***p***-Si, and ITO/***p***-Si structures taken at bias voltage of ±5 V, where photocurrents are obtained by the difference of currents under illumination and darks. The latter two structures represent devices with a capping layer of undoped MS and even without a capping layer. In this spectrum, the wavelength dependence of transparency and reflectivity of ITO has been considered. Reverse (forward) photoresponse in ITO/nc-Si-embedded MS/***p***-Si at 325-nm, 425-nm, and 590-nm are calculated to be of 0.2 (0.04) A/W, 0.4 (0.1) A/W, and 0.9 (0.17) A/W, respectively, which gives a rectifying ratio of about 4-5. A reversal in rectifying behavior is independent of illumination intensity if the dark signal had been considered (See ***I-V*** curves for 325-nm light of 1mW and 3 mW, and 632-nm light of 0.3 mW). Low dark currents with high dynamic resistance of 1.3 MΩ and high photoresponse gives high detectivity of ~$2x10^{12}$ $cm.Hz^{0.5}W^{-1}$ [11], this value is of the order of magnitude of common Si photodiodes.

The broad band feature (350-700 nm) in PL spectra of nc-Si-embedded MS are associated with the chemical bonds to be extremely complex with various bonding geometries at the interfaces of nc-Si and MS. As a result, photoresponse covers UV to visible bands despite the existence of a major blue band-gap in nc-Si-embedded MS. Closely examining all spectral-dependent photoresponse curves reveals that the capped nc-Si-embedded MS actually enhances reverse photocurrents. Moreover, gain in reverse photocurrents of 1-2, where quantum efficiency is assumed as one, was observed.

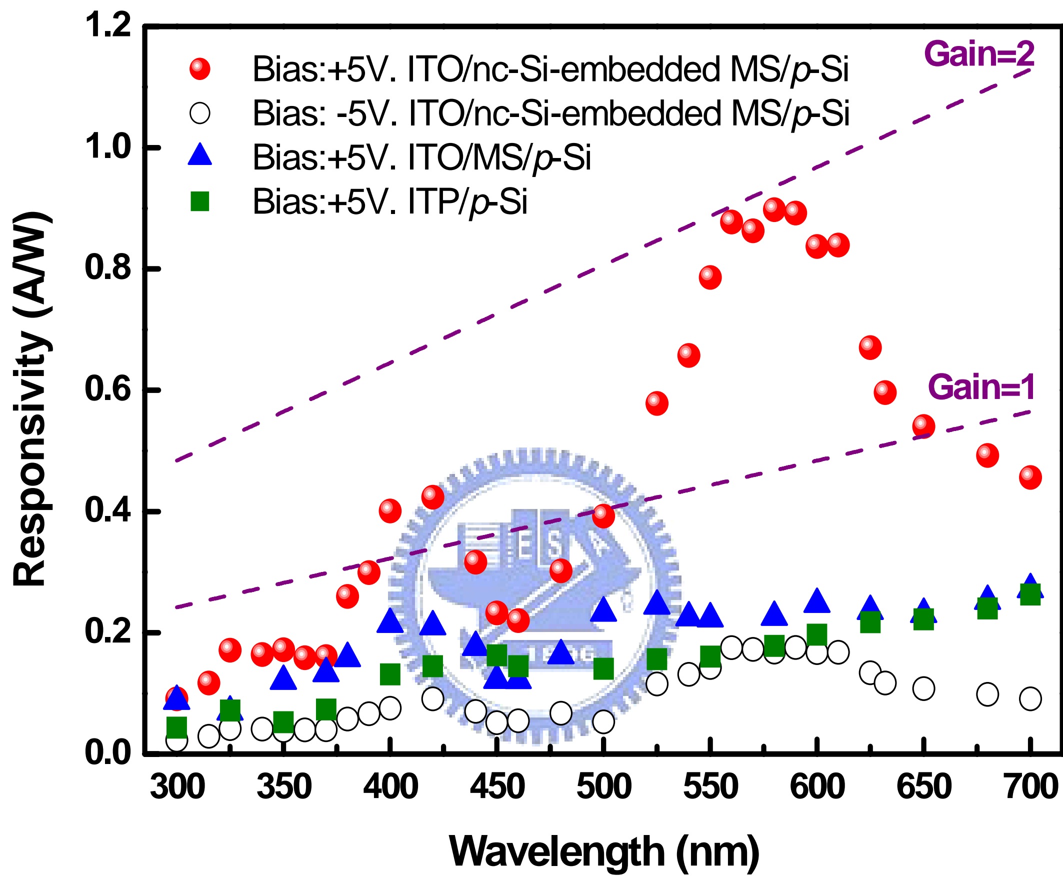

Fig. 4.5 Spectral dependence of photoresponse in ITO/nc-Si-embedded MS/***p***-Si, ITO/MS/***p***-Si, and ITO/***p***-Si structures.

4.4 Results of illumination intensity dependence of photocurrent

The illumination intensity dependence of photocurrent in ITO/nc-Si-embedded MS/***p***-Si structures for 325-nm of 0.56~11.2mW, and 632-nm light of 0.56~5.6mW are shown in Fig. 4.6, 4.8, respectively. With different powers, the saturated voltage also increases. This is due to high power causes larger channel width and yields higher currents. Fig. 4.7 and fig. 4.9 also show the illumination intensity dependence of photocurrent in our devices at 325-nm light, and 632-nm light, respectively. The relationship between the photocurrent and the illumination intensity is linear at certain bias voltage 5 V under 325-nm illumination. Note that under forward bias of negative voltage, the current is reduced when the sample is illuminated while under reverse bias of negative voltage it is increased. This effect is explained by charging of nanocrystals in the oxide layer by photo-ionization of electrons [12].

Current transport in conventional MIS structures is mainly due to majority carriers (holes in ***p***-type substrate) in forward bias [13] but in reverse bias minority carriers (electrons) in the inversion layer at the oxide–silicon interface can dominate conduction [14]. With uniform illumination, the equilibrium concentrations of electrons and holes are increased. The extra minority carriers (electrons) caused by photon absorption in the inversion layer at reverse biases of positive voltage leads to an increase in current. So, at reverse bias, the response to illumination is as expected, the current increases by the illumination intensity increasing, as shown in Fig. 4.6 or 4.8. However, under forward bias conditions, the current under higher illumination intensity is smaller than the lower illumination intensity for the ITO/nc-Si-embedded MS/***p***-Si structures, as shown in Fig. 4.7 or 4.9. As discussed above, this phenomenon is known as negative photoconductivity.

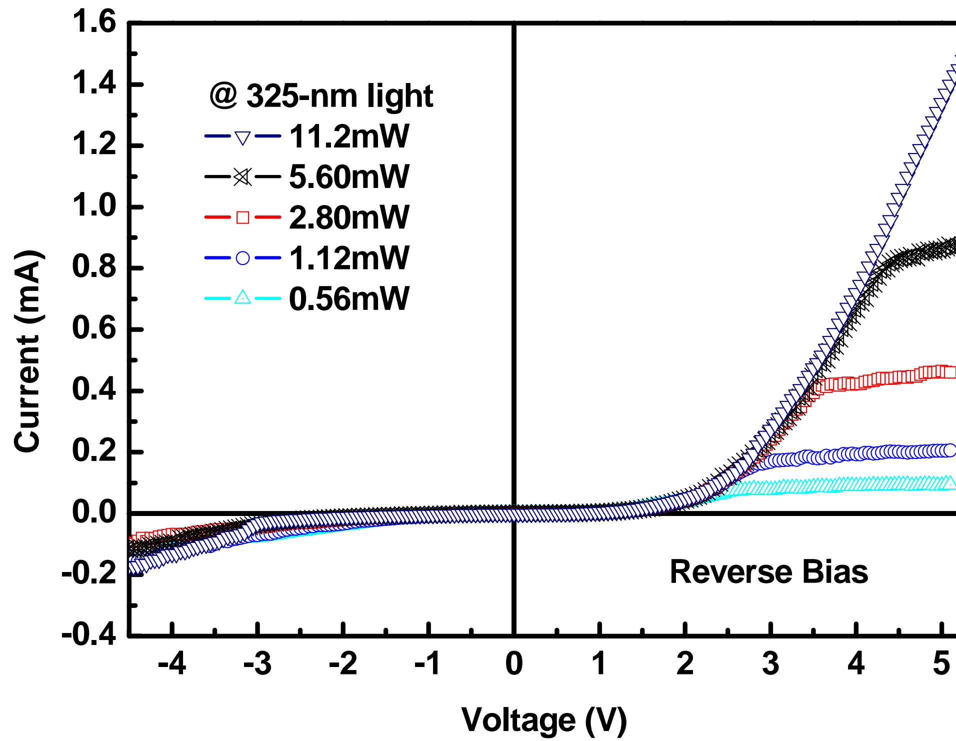

Fig. 4.6 Current-voltage characteristics of ITO/nc-Si-embedded MS/***p***-Si devices irradiated with 325-nm light of 0.56~11.2mW.

1896

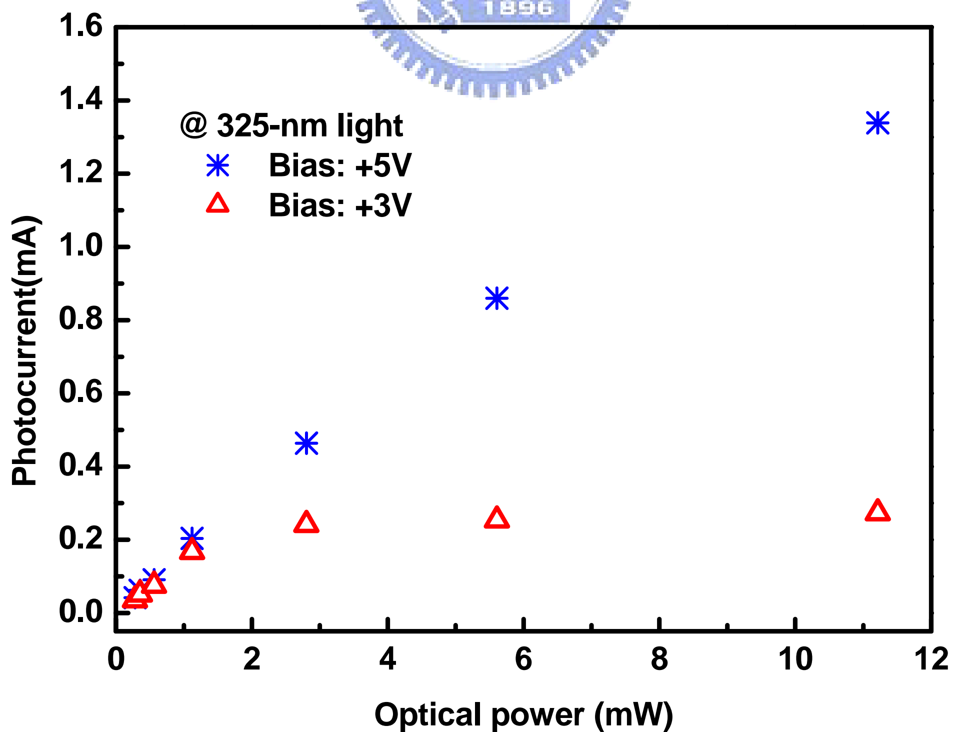

Fig. 4.7 Illumination intensity dependence of photocurrent in ITO/nc-Si-embedded MS/***p***-Si devices at 325-nm light.

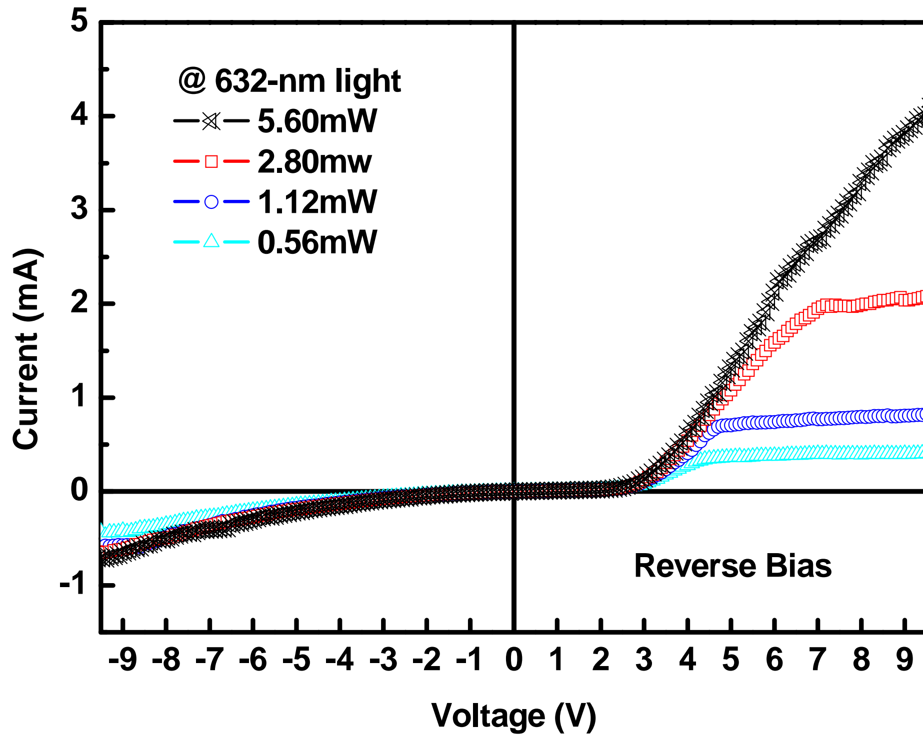

Fig. 4.8 Current-voltage characteristics of ITO/nc-Si-embedded MS/***p***-Si devices irradiated with 632-nm light of 0.56~5.6mW.

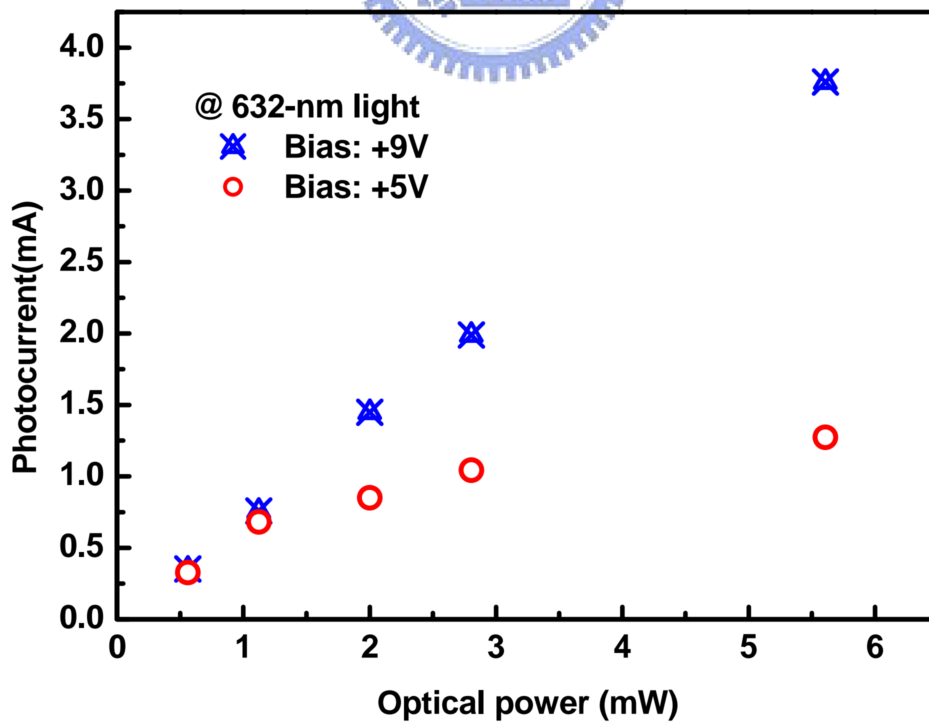

Fig. 4.9 Illumination intensity dependence of photocurrent in ITO/nc-Si-embedded MS/***p***-Si devices at 632-nm.

The following explanation is proposed to account for negative photoconductivity in the present sample. Taking this into account we depicted schematically the band structure of the ITO/nc-Si-embedded MS/***p***-Si devices in figure 4.10. The MS has a high density of states, no depletion should occur at the ITO-MS interface. This contact should behave almost in an ohmic manner. On the other hand, the high density of states might pin the Fermi level at the other hetero-junction, the MS-*p*-Si boundary. This should result in a band bending and depletion inside the ***p***-Si [9], as shown in figure 4.10. The short lines are localized electronic states, some of which are occupied (circles).

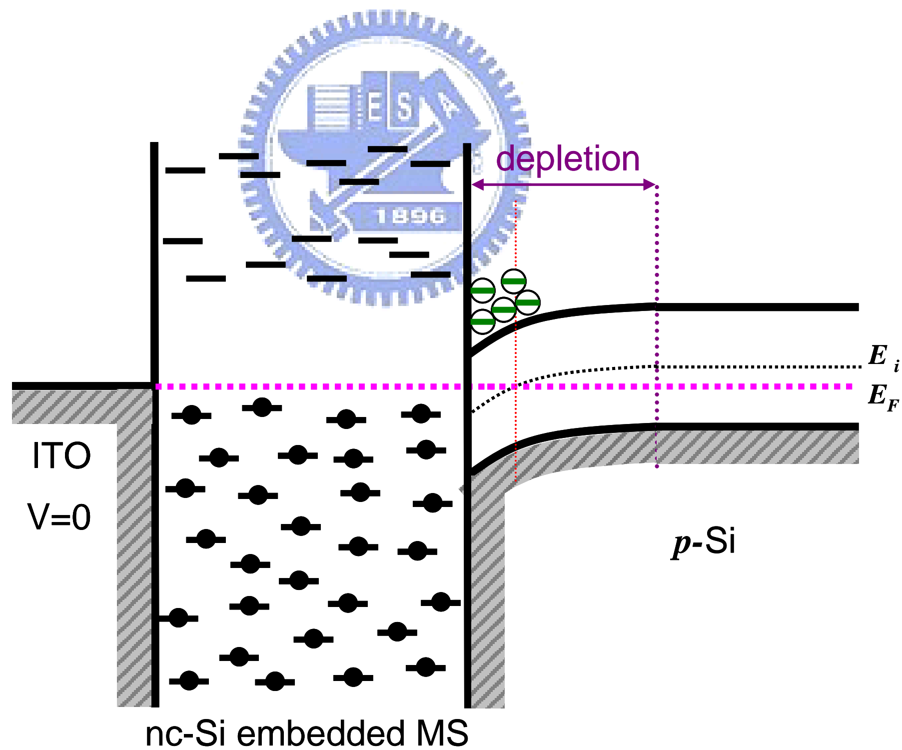

Fig. 4.10 A schematic band diagram of ITO/nc-Si-embedded MS/***p***-Si devices in equilibrium.

When the devices is illuminated, photoexcited electron/hole pairs generate firstly, then photoionized electrons transport from the nc-Si-embedded MS layer to ***p***-Si by resonant tunneling and recombine with holes in the accumulation layer formed at the MS-***p***-Si interface under forward bias (steps 1-3 of Fig. 4.11). Nanocrystals in the oxide are then positively charged by the remaining holes. These positive charges screen the applied forward bias of negative voltage, resulting in a decrease of the current at a certain voltage (step 4 of Fig. 4.11). If the current decrease caused by this effect is larger than the current increase caused by the photoexcitation of extra holes in the accumulation layer, negative photoconductivity is observed.

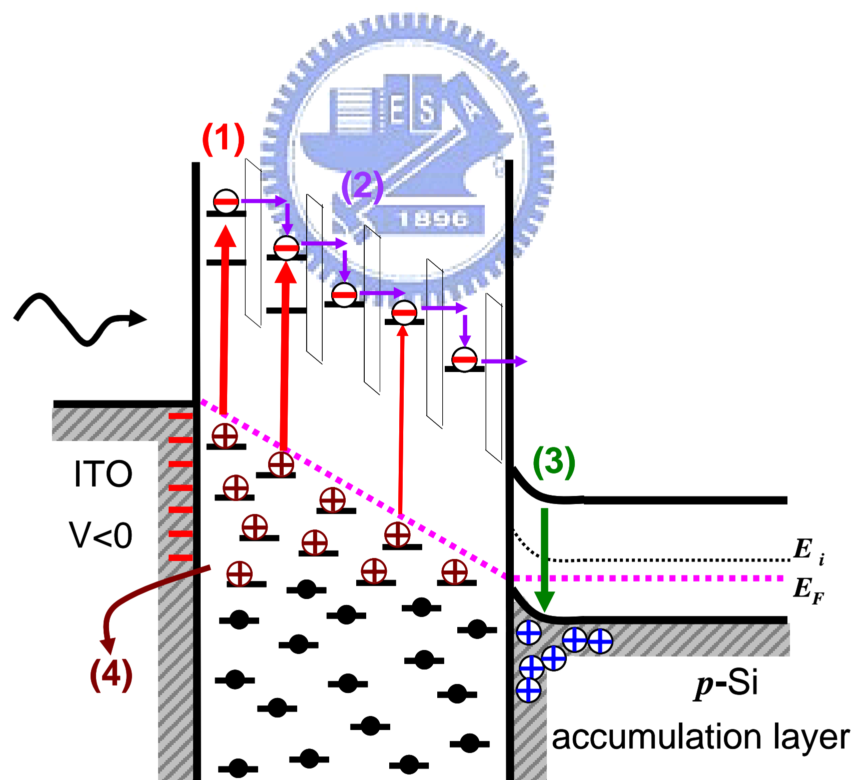

Fig. 4.11 Band diagram in irradiated ITO/nc-Si-embedded MS/***p***-Si under forward bias.

4.5 Results of temporal response

The photocurrent transients of ITO/nc-Si-embedded MS/***p***-Si detectors illuminated by 420-nm, 590-nm, and 640-nm light of 1 mW at bias 5V shows that the photocurrent decays with a time constant of about 10 ns corresponding to a 3 dB bandwidth of 16 MHz under different illuminated wavelength, as shown in Fig. 4.12. The transit time it takes for carriers to traverse the film τ_t is described by the equation

$$u_{eff} = \frac{d^2}{\tau_t V} \quad \left(\frac{cm^2}{s \cdot V}\right)$$

where V is the applied bias, d is the film thickness, and u_{eff} is the effective mobility. This relationship assumes a single electron-hole mobility, although the argument is essentially the same if the mobilities are unequal. Silicon nano-particles films in similar devices report a u_{eff} on the order of 10^{-3} cm^2/V s [15]. This direct correlation demonstrates that improvements in device performance will require increased carrier motion through the silicon nanostructures. From the above equation, we estimate the effective mobility is 1.25x 10^{-2} cm^2/V s for our devices.

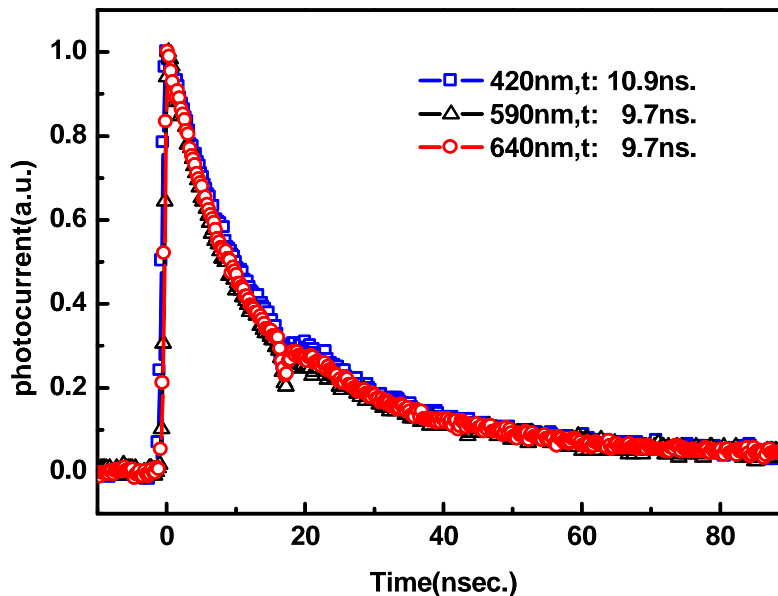

Fig. 4.12 Photocurrent transients of ITO/nc-Si-embedded MS/***p***-Si detectors illuminated by 420-nm, 590-nm, and 640-nm light of 1 mW.

4.6 Discussion

Comparing photodiodes fabricated with Si-particle [15] and porous Si thin films [16,17] are constructive in determining the gain mechanism in our device. Highly resistive porous Si essentially dominates photocurrents with no gain. Nayfeh *et al.* [15] demonstrated photoconductive gain in forwardly biased Si-particle UV detectors due to reduced transient time originated from enhanced carrier mobility by resonant tunneling among dense Si-particles. Photoresponse in our device was found to be independent of illuminated light intensity in the range of 60-1000 W/m^2 (See Fig. 4.7 or Fig. 4.9) [18]. Figure 4.12 shows response time as fast as ten nanoseconds, much quicker than these demonstrated by photoconductive detectors [15,19]. Hence, photoconductive gain was barely involved in an enhancement of reverse photocurrents of ITO/nc-Si-embedded MS/***p***-Si. [15,18,19]. A gain mechanism, barrier lowering by photo-induced charging of surface states, normally reveals larger gain in forward photocurrents than in reverse photocurrents [20], as opposed to our observations.

Choi *et al.*[12] found a reduction in forward currents under irradiated nc-Si-embedded SiO_2 as a result of the screening of applied forward bias of negative voltage by the charging of hole in nc-Si as photoionized electrons recombines with holes in the accumulation layer. Note that the shift of energy level in the conduction band is larger than that in the valence band as the result of a quantum confinement effect in the silicon nanostructures [21]. Therefore, the tunneling barrier for electrons in nc-Si or even nc-Si/silica is lowered to a considerable extent, compared to that for holes. Photoionized electrons thus more easily transport than photoionized holes in nc-Si-embedded MS. It also facilitates the formation of positively charged nc-Si-embedded MS layers even as an inversion layer in ***p***-Si substrates under reverse bias appears. In this manner, an applied reverse (forward) bias of positive (negative)

voltage was enhanced (screened) by such a photo-induced positively charged layer (**PIPCL**) so as to initiate an avalanche-like process (a limited photoconductive process) [12], giving gain (saturation) in reverse (forward) photocurrent, as schematically depicted in Fig. 4.13. Under reverse bias reveals an enhancement of reverse photocurrents due to the formation of positively charged layers of nc-Si-embedded MS films, where photoexcited electron/hole pairs generate firstly, then photoionized electrons occurs, and eventually hole charging in Si-O nanostructures enhances applied reverse bias of positive voltage (Steps 1-2), while initiating impact ionization in a avalanche manner to generate extra carriers to transport to top electrodes by resonant tunneling among dense Si nanocrystals or numerous nc-Si/silica interfaces (Steps 3-4). Notably, dense and uniform Si nanocrystals in MS matrix also assist resonant tunneling. As expected, in ITO/MS/***p***-Si, the effect of PIPCL is greatly reduced in teams of reduced rectifying ratio of 1.3-1.5 in photocurrents and no gain (See Fig. 4.5), due to the absence of nc-Si.

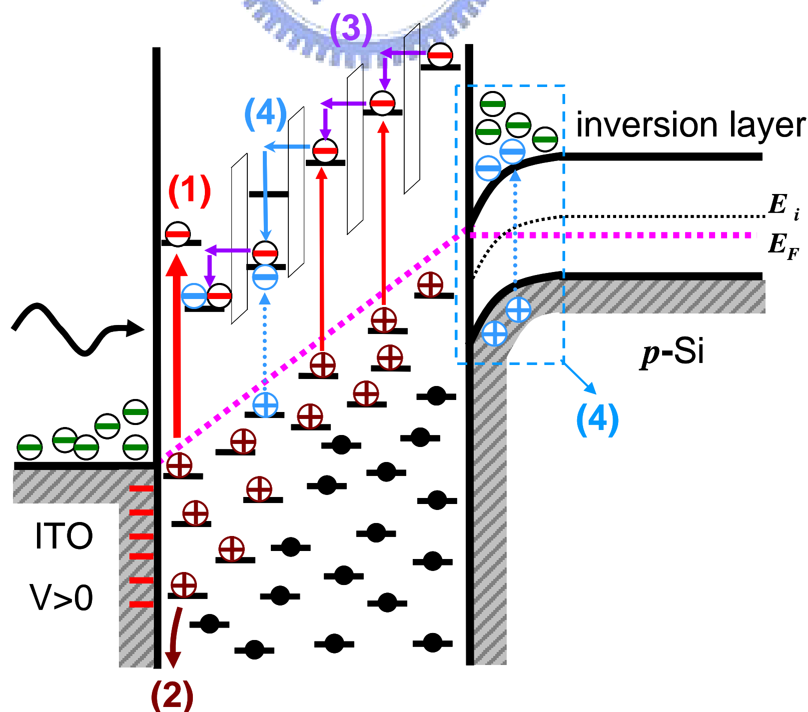

Fig. 4.13 Band diagram in irradiated ITO/nc-Si-embedded MS/***p***-Si under reverse bias.

As light wavelength becomes shorter, more illumination energy was expected to be absorbed by the nanostructured film of nc-Si-embedded MS such that a larger net reverse bias established but fewer numbers of photocarriers generated in the regions of nc-Si-embedded MS/***p***-Si interface and in ***p***-Si substrates. Furthermore, large absorption coefficient (1.5-3x10^4 cm^{-1}) in thick nc-Si-embedded MS films at short wavelength (300-450 nm) likely appreciably increases the loss in photocurrents at UV wavelength through recombination of photocarriers [19]. These factors result in a maximum photoresponse of 0.9 A/W at 590 nm and give a spectral photoresponse with two peaks as seen on Fig. 4.5 even though the photoresponse at the UV band is as high as 0.2-0.4 A/W.

4.7 References

1. A. T. Cho, J. M. Shieh, J. Shieh, Y. F. Lai, B. T. Dai, F. M. Pan, H. C. Ku, Y. C. Lin, K. J. Chao, and P. H. Liu, *Electrochem. Solid-State Lett.* **8**, G143 (2005).
2. D. P. Yu, Q. L. Hang, Y. Ding, H. Z. Zhang, Z. G. Bai, J. J. Wang, Y. H. Zou, W. Qian, G. C. Xiong, and S. Q. Feng, *Appl. Phys. Lett.* **73**, 3076 (1998).
3. M. S. EI-Shall, S. Li, T. Turkki, D. Graiver, U. C. Pernisz, and M. I. Baraton, *J. Phys. Chem.* **99**, 17806 (1995).
4. J. Y. Zhang, X. M. Bao, Y. H. Ye, and X. L. Tan, *Appl. Phys. Lett*. **73**, 1790 (1998).
5. Y. D. Glinka, S. H. Lin, L. P. Hwang, and Y. T. Chen, *Appl. Phys. Lett.* **77**, 3968 (2000).
6. Y. Zhang, F. Phillipp, G. W. Meng, L. D. Zhang, and C. H. Ye, *J. Appl. Phys.* **88**, 2169 (2000).
7. T. A. Burr, A. A. Seraphin, E.Werwa, and K. D. Kolenbrander, *Phys. Rev. B* **56**, 4818 (1997).
8. M. A. Rafiq, Y. Tsuchiya, H. Mizuta, S. Oda, Shigeyasu Uno, Z. A. K. Durrani, and W. I. Milne, *Appl. Phys. Lett.* **87**, 182101 (2005).
9. M. Ben-Chorin, F. Moller, and F. Koch, *J. Appl. Phys.* **77**, 4482 (1995).
10. Z. Shen, U. Kortshagen, and S. A. Campbell, *J. Appl. Phys.* **96**, 2204 (2004).
11. C. K. Wang, T. K. Ko, C. S. Chang, S. J. Chang, Y. K. Su, T. C. Wen, C. H. Kuo, and Y. Z. Chiou, *IEEE Photon. Technol. Lett.* **17**, 2161 (2005).
12. S. H. Choi and R. G. Elliman, Appl. Phys. Lett. **74**, 3987 (1999).
13. P. Cova, A. Singh, and R. A. Masut, *J. Appl. Phys.* **82**, 5217 (1997).
14. S. M. Sze, *Physics of Semiconductor Devices*, 2nd ed. (Wiley, New York, 1981),
15. O. M. Nayfeh, S. Rao, A. Smith, J. Therrien, and M. H. Nayfeh, *IEEE Photon. Technol. Lett.* **16**, 1927 (2004).
16. J. P. Zheng, K. L. Jiao, W. P. Shen, W. A. Anderson, and H. S. Kwok, *Appl. Phys. Lett.* **61**, 459 (1992).
17. M. K. Lee, C. H. Chu, Y. H. Wang, S. M. Sze, *Optics Letters*, **26**, 160 (2001).
18. S. K. Zhang, W. B. Wang, I. Shtau, F. Yun, L. He, H. Morkoc, X. Zhou ,M. Tamargo, and R. R. Alfano, *Appl. Phys. Lett.* **81**, 4862 (2002).
19. S. M. Sze, *Physics of Semiconductor Devices*, 2nd ed. (Wiley, New York, 1981), pp.743-770.
20. O. Katz, V. Garber, B. Meyler, G. Bahir, and J. Salzman, *Appl. Phys. Lett.* **79**, 1417 (2001).
21. N. M. Park, S. H. Jeon, H. D. Yang, H. Hwang, S. J. Park, and S. H. Choi, *Appl. Phys. Lett.* **83**, 1014-1016 (2003).

Chapter 5 Conclusions and future works

5.1 Conclusions

Three-dimensional dispersed Si nanocrystals (NCs) were dispersed within the mesoporous silica films by inductively coupled plasma chemical vapor deposition **(ICPCVD)**. ICP makes reactive species own highly mobile and bond with pore-wall well, therefore, efficiently construct 3D Si NCs/silica arrays. The mean density of ICP-synthesized NCs is as high as $2.5x10^{18}/cm^3$. The specific interfacial bond-induced wide-bandgap electronic structure in nanostructured film significantly enhances the light extraction efficiency and the conduction of photoexcited carriers.

We constructed efficient UV-visible ITO/nc-Si-embedded MS/***p***-Si detectors based on Si nanomaterials by thin film technology. The capping layer is consisted of three-dimensional array of Si nanocrystals embedded in a mesoporous silica matrix was integrated in the IC-compatible configuration of metal-oxide-semiconductor. The photodetectors revealed a responsivity of 0.4 A/W and 0.9 A/W for 420-nm and 590-nm at reverse bias 5V, respectively. Low dark currents with high dynamic resistance of 1.3 MΩ and high photoresponse gives high detectivity of $\sim 2x10^{12}$ $cm.Hz^{0.5}W^{-1}$. Temporal response at bias 5V shows that the photocurrent decays with a time constant of about 10 ns corresponding to a 3 dB bandwidth of 16 MHz under illuminated by 420-nm, 590-nm, and 632-nm light of 1 mW.

5.2 Future works

In order to form Si-nanodot photoconductive films with carrier multiplication at a low electric field and photoresponse at various wavelengths, the Si nanodots with a uniform dot size distribution are necessary, because the dot size fluctuation brings about a variation in the band gap of the dots. To obtain higher responsivity and shorter transit time for stacked layer structures of Si nanodots in short wavelength, controlling the dot density, smaller dot size, and the oxide thickness are of great importance. MSM structure can reduce the loss of absorption and transit time to improve the characteristic of devices.